

A Large Eddy Simulation model for the study of wind turbine interactions and its application

M. Draper^{1,*}, A. Guggeri¹, M. Mendina¹, G. Usera¹, and F. Campagnolo²

¹Facultad de Ingeniería, Universidad de la República, Julio Herrera y Ressig 565,
Montevideo, Uruguay.

²Wind Energy Institute, Technische Universität München, Boltzmannstraße 15, D-85748
Garching bei München, Germany.

*Corresponding author: mdraper@fing.edu.uy

Abstract

Wind energy has become a mature technology in the past decade, nevertheless there are still open challenges to continue its growth and development. Recently, there has been an increasing interest in the academic community as well as in the industrial sector about the operation and control of a wind farm at a farm level. This new paradigm has different purposes, from maximizing power production through wake modulation to active power control. Different strategies, from physical experimentation to numerical simulation, have been developed to do research in this field. The aim of the present paper is to present results of a validated numerical method applied to the simulation of a state of the art experimental setup. Two setups subject to an atmospheric boundary layer like inflow condition are simulated, a stand alone model wind turbine without torque controller and three model wind turbines with a non-greedy yaw setting. An acceptable agreement is obtained between the experimental data and the numerical results, showing an interesting complementary approach between physical and numerical simulation.

1 Introduction

Wind energy has expanded globally in the past few decades, becoming a mature technology, achieving almost 466 GW of installed capacity [1]. This development of wind energy has been supported by technological improvements which are related to an increase in hub height, rotor diameter and unit power, which has led to larger capacity factors for the same wind speed [2]. Nevertheless, there are still open challenges to continue its growth and development. Low, medium and high fidelity models, as well as laboratory and full-scale measurements, are complementary strategies [3], that should be combined.

Computational fluid dynamic codes represent the state of the art to simulate with high fidelity the flow through wind turbines. Two approaches exist in order to represent the presence of a wind turbine in a simulation [4]: 1) actuator models, in which the blades are represented as body forces, 2) direct representation of the blade's geometry through the computational mesh. Among the actuator models, the Actuator Line Model (ALM), introduced in [5], has been widely validated (please see for instance [6, 7, 8, 9, 10, 11, 12]), showing to reproduce accurately the wind flow in the wake of a wind turbine with moderate computational cost as compared to direct representation. Despite this, it is still a hard task to accurately simulate the wind flow through a stand alone wind turbine and wind farms, characterizing the wakes as well as calculating integral quantities as power and thrust coefficients, as it can be seen in the different blind tests developed in the past few years [13, 14, 15, 16].

Recently, the authors have evaluated the ALM with coarser spatial resolutions and also larger time steps than what is generally recommended, considering an uniform inflow condition [17] as well as an Atmospheric Boundary Layer (ABL) like inflow condition. For the latter three validation cases have been assessed: Horns Rev offshore wind farm, a 7.7 MW onshore wind farm in Uruguay and a well-known wind tunnel campaign

[18, 19, 20], finding a good agreement with the SCADA (Supervisory Control And Data Acquisition) data in the power deficits in [18, 19] and accuracy to reproduce the wake of the model wind turbine in [20].

Several studies combine numerical simulation and wind tunnel experimental campaigns. For example, in [21] a stand-alone model wind turbine placed in a wind tunnel and subject to an ABL like inflow condition is simulated with different actuator models to represent the wind turbine rotor, finding a good agreement in the main characteristics of the wake. This experimental campaign has been simulated by other authors, see for instance [20, 22]. A similar experimental setup, but studying the wind flow through and above an array of model wind turbines, is simulated in [23] taking into account different layouts. The experimental campaigns used in the different blind tests mentioned above have been simulated by different research groups, for example Blind Test 1 [13] has been simulated in [24, 17], Blind Test 2 [14] in [17], Blind Test 4 [16] in [10]. Regarding the experimental data considered in this work, tests were conducted within the boundary layer wind tunnel of the Politecnico di Milano [25]. A scaled wind farm, composed of three wind turbine models already used within other research projects [26, 27, 28], has been employed, together with two synchronized scanning LiDARs, to generate part of the results discussed in this paper.

The aim of the present paper is to present results of a validated numerical method applied to the simulation of a state of the art experimental setup, that has not been widely simulated. Two setups subject to an atmospheric boundary layer like inflow condition are simulated, a stand alone model wind turbine without torque controller and three model wind turbines with torque controller and a non-greedy yaw setting. The paper is organized as follows: Section 2 presents the solver and the ALM implementation, Section 3 describes the experimental setup, Section 4 presents the main results and summary is given in Section 5. A manuscript with further results have been submitted and it is under review.

2 Numerical Method

2.1 Flow solver

caffa3d.MBRi is an open source finite volume code, second order accurate in space and time. A brief presentation of the solver is given in this Section, for further information and validation examples please see [29, 30].

The domain is divided in unstructured blocks of structured grids, using a collocated arrangement. The same block structure is used for parallelization through MPI by domain decomposition. The mathematical model comprises the mass balance equation (1) and momentum balance equation (2) for a viscous incompressible fluid, together with generic passive scalar transport equation (3) for scalar field ϕ with diffusion coefficient Γ . Note that (2) has been written only for the first Cartesian direction \hat{e}_1 . The balance equations are written for a region Ω , limited by a closed surface S , with outward pointing normal \hat{n}_S .

$$\int_S (\vec{v} \cdot \hat{n}_S) dS = 0 \quad (1)$$

$$\int_{\Omega} \rho \frac{\partial u}{\partial t} d\Omega + \int_S \rho u (\vec{v} \cdot \hat{n}_S) dS = \int_{\Omega} \rho \beta (T - T_{ref}) \vec{g} \cdot \hat{e}_1 d\Omega + \int_S -p \hat{n}_S \cdot \hat{e}_1 dS + \int_S (2\mu D \cdot \hat{n}_S) \cdot \hat{e}_1 dS \quad (2)$$

$$\int_{\Omega} \rho \frac{\partial \phi}{\partial t} d\Omega + \int_S \rho \phi (\vec{v} \cdot \hat{n}_S) dS = \int_S \Gamma (\nabla \phi \cdot \hat{n}_S) dS \quad (3)$$

where $\vec{v} = (u, v, w)$ is the fluid velocity, ρ is the density, β is the thermal expansion factor, T is the fluid temperature and T_{ref} a reference temperature, \vec{g} is the gravity, p is the pressure, μ is the dynamic viscosity of the fluid and D is the strain tensor.

The generic transport equation (3) for passive scalars can be used to implement, in a straightforward manner, further physical models like heat transport, turbulence models, etc. The use of equations in their global balance form, together with the finite volume method, as opposed to the differential form, favors enforcing conservation properties for fundamental magnitudes as mass and momentum into the solving

procedure [31].

The global grid is made up from structured grid blocks, which can be either orthogonal Cartesian grid blocks or curvilinear body fitted grid blocks. Nevertheless, geometrical and flow properties are always expressed in a Cartesian coordinate system, expressing flow properties in primitive variables. To provide greater geometrical flexibility, the immersed boundary method [32] can be combined with both, Cartesian and body fitted grid blocks. In addition to this, an overlapping grid technique based on [33] is implemented in the code, allowing for independent grids with higher quality where it is required.

Each equation in the mathematical model is discretized and linearized at each cell to obtain a discrete approximation in the form of (4), written again for the u velocity component, where the variable value at each cell center is related to the values at the six neighbors. Further details for discretization of each term will not be given here but can be found in [29, 30], together with validations of the solver.

$$A_P^u \cdot u_P + A_W^u \cdot u_W + A_E^u \cdot u_E + A_S^u \cdot u_S + A_N^u \cdot u_N + A_B^u \cdot u_B + A_T^u \cdot u_T = Q_P^u \quad (4)$$

A block structured variant of the Stone-SIP solver algorithm [34] that accommodates well to the block structure inherited from the grid, is used. This allows efficient parallelization through MPI.

To deal with the linearization and subsequent coupling of linear systems for each equation in the mathematical model, an outer-inner iteration scheme for each time step is employed, as shown in Figure 1. Linear systems for each equation in the mathematical model are sequentially assembled and undergo inner iterations with SIP or AMG-SIP linear solvers. The outer loop is repeated within each time step until the desired level of convergence is achieved before continuing to the next time step. Regarding the turbulence model,

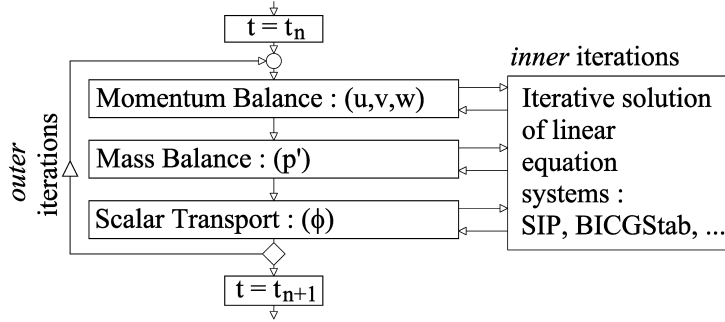


Figure 1: Iteration scheme for one time step (adapted from [31]).

different subgrid scale models in the context of Large Eddy Simulation (LES) are implemented: the standard Smagorinsky model [35] with damping function for smooth [31] and rough surfaces [36], the dynamic Smagorinsky model [37] with different averaging schemes, the dynamic mixed Smagorinsky model [38] and the scale-dependent dynamic Smagorinsky model [39] with different averaging schemes.

2.2 Actuator Line Model

In the ALM, the wind turbine rotor is represented as a body force field, instead of resolving the blade boundary layers, each blade is represented as a line that moves with the rotational speed of the rotor and it is discretized in radial sections where the aerodynamic forces are computed (Figure 2, left). To compute the force in each radial section, geometrical properties (chord length and twist angle) as well as aerodynamic properties (lift and drag coefficients) are found. The latter are obtained from tabulated airfoil data. At each radial section the aerodynamic force is computed as

$$\vec{f} = -\frac{1}{2}\rho V_{rel}^2 c (C_L \vec{e}_L + C_D \vec{e}_D) dr \quad (5)$$

where ρ is the air density, V_{rel} is the relative velocity, c is the chord length, C_L is the lift coefficient, C_D is the drag coefficient, \vec{e}_L is a unit vector in the direction of the lift force, \vec{e}_D is a unit vector in the direction of the drag force (Figure 2, right) and dr is the length of the radial section. Prandtl's tip loss correction factor

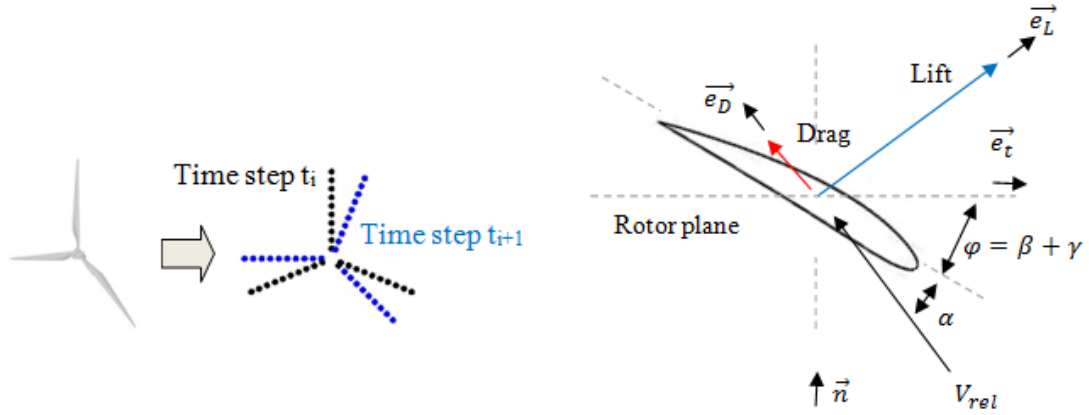


Figure 2: ALM rotor representation (left) and a cross-sectional airfoil radial section (right).

is applied, as it has shown to improve the results [17]. A Gaussian smearing function (6) is used to project the aerodynamic forces onto the computational domain, taking into account three smearing parameters, one for each direction (n normal, r radial and t tangential) as described in [18].

$$f(d_n, d_r, d_t) = \frac{1}{\epsilon_n \epsilon_r \epsilon_t \pi^{1.5}} e^{-\left(\frac{d_n}{\epsilon_n}\right)^2} e^{-\left(\frac{d_r}{\epsilon_r}\right)^2} e^{-\left(\frac{d_t}{\epsilon_t}\right)^2} \quad (6)$$

3 Experimental setup

The experimental setup is shown in Figure 3. It consists of 3 wind turbine models, in the following named G1s, whose rotor diameter D is 1.1 m and which were separated $4D$ in the streamwise direction and with a lateral shift of half a diameter. The same figure also depicts the two short-range WindScanners which were employed to get a reliable high resolution mapping of the wind field. Local flow measurements obtained by hot-wire probes were also used to validate the results shown in Section 4.

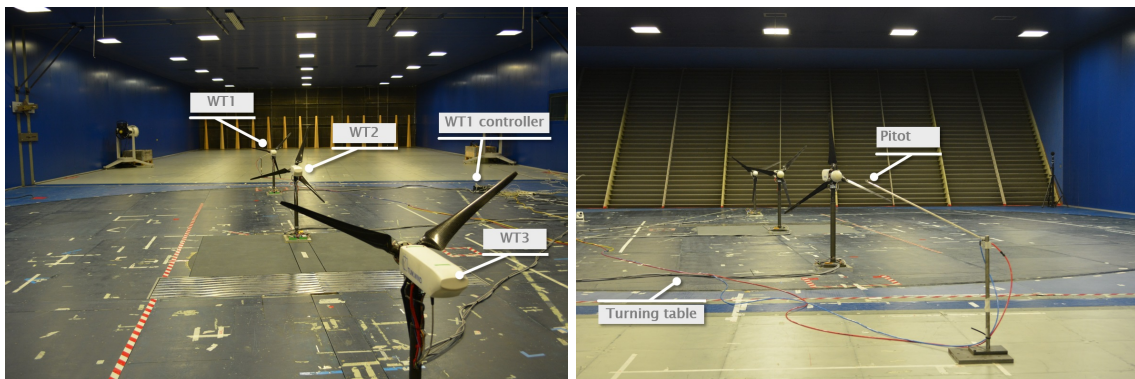


Figure 3: Wind farm layout in the wind tunnel.

3.1 Wind turbine models

Each G1 (see Figure 4) is equipped with a three-blades rotor whose maximum rotating speed is 850 rpm. Each carbon-made blade, mounted on the hub with two bearings, houses, within its hollow root, a small brushed motor equipped with a gear-head and a built-in relative encoder. This system enables, together

with a dedicated electronic control board housed in the hub spinner, the individual pitch angle variation of the blade.

The rotor is connected with three small screws to the main shaft, whose torsional and bending loads are measured by means of strain gauges glued on four CNC-machined small bridges. Three miniaturized electronic boards, fixed to the hub and rotating with it, provide for the power supply and conditioning of the shaft strain gauges. The shaft is held by two bearings and after them there is a torque-meter, which enables the measurement of the torque provided by the generator, located in the rear part of the nacelle and managed by a dedicated servo-controller. An optical encoder, located between the slip ring and the rear shaft bearing, allows for the measurement of the rotor azimuth. In order to enable the accurate measurement

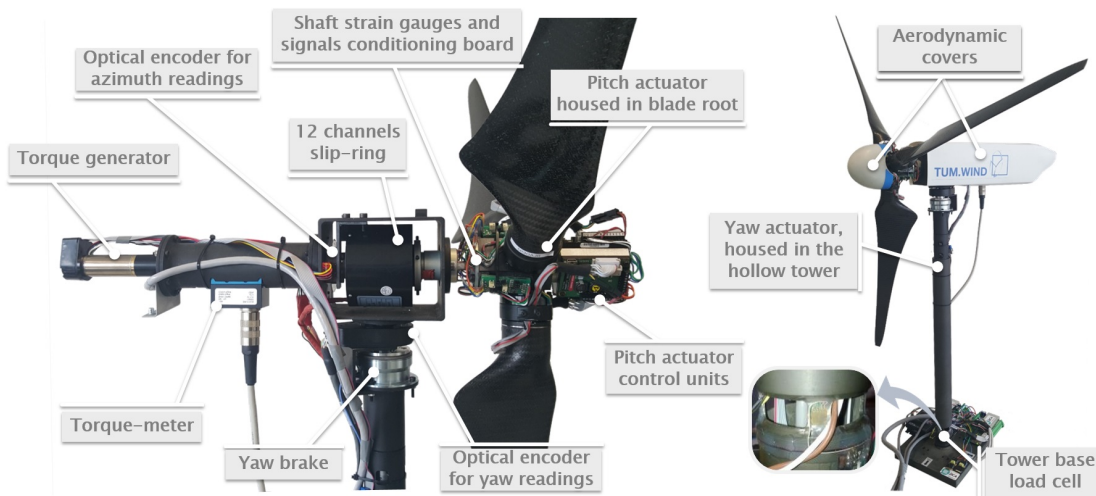


Figure 4: Layout of G1 model.

of the loads at the tower base, strain gauges were glued on four small bridges machined close to the base and sized so as to have sufficiently large strains. Two electronic boards provide for the power supply and adequate conditioning of this custom-made load cell.

A brushed motor, housed within the hollow tower top and equipped with a gear-head, allows for the complete yawing of the entire nacelle. To this aim, an optical encoder provides feedback to an electronic device that controls both the yaw actuator and a magnetic brake. Finally, aerodynamic covers of the nacelle and hub ensure a satisfactory quality of the flow in the central rotor area

Each model is controlled by a *M1 Bachmann* hard-real-time module. Similarly to what is done on real wind turbines, the *M1* implements collective or individual pitch-torque control laws, similar to the ones described in [40] and references therein.

The performance of the **G1** rotor, whose blades are equipped with the low-Reynolds airfoil RG14 [41], was measured for different values of the airfoil Reynolds numbers (between 50-90000) and at several combinations of TSR and collective pitch settings. The measured maximum power coefficient is approximately 0.42 at $\lambda \in [7, 8]$ and $\beta \in [-2^\circ, 0^\circ]$.

Significant differences were noticed between the measured and theoretical Blade Element Momentum (BEM)-based aerodynamic performance computed using nominal polars. This problem is probably due to inaccuracies in the airfoil performance computation, in turn due to the challenges associated with the prediction of the laminar bubble separation at very-low Reynolds number. To correct for this, an identification procedure [42] was used to calibrate the polars, leading to the satisfactory agreement shown in other publications [12, 43].

The undisturbed wind speed was measured by means of a Pitot tube, also shown in Figure 3, placed at hub height in front of the upstream model.

3.2 Short-range LiDARs

Each of the two short-range LiDARs was installed near the walls of the tunnel, approximately 7D upwind of the turbine models. The LiDARs provided averaged wind speeds at rates up to 390 Hz. They were both equipped with two prism motors and a focus motor, which enabled steering the laser beam within a cone of 120° of aperture. A common central motion controller ensured that the two focused laser beams were synchronously following a common scanning trajectory. A complete description of the system, as well as the demonstration of its potential when applied to the measurement of small scale flow structures in a wind tunnel, is given in [44].

Three LiDAR systems with three linearly independent beam directions would be necessary to measure the three-dimensional flow velocity vector. Given the distance from the LiDARs and the points of measurement, as well as considering that LiDAR heads are located slightly above the turbine hub height, the plane created by the LiDAR beams is mostly horizontal ($\pm 3^\circ$). It can therefore be assumed that, from two temporally and spatially synchronised line-of-sight measurements, one can derive the components of the flow speed along and laterally to the main wind direction, with an insignificant contamination of the result by the vertical wind speed component [44].

4 Simulation cases and results

In this Section the different simulation cases considered are presented, first introducing the numerical setup used and then describing the main results obtained.

4.1 Stand-alone model wind turbine

A scale model wind turbine G1, described in Section 3, is simulated subject to an ABL like inflow condition, with a mean streamwise velocity component of 5.0 m/s at hub height and turbulence intensity of approx. 5.5%. The vertical profile of the mean streamwise velocity component is characterized by a power law with shear exponent of 0.09. The model wind turbine operates at fixed pitch angle and fixed angular velocity (without torque controller).

4.1.1 Numerical setup

The size of the computational domain is 27.50 m in the streamwise direction, 5.50 m in the spanwise direction and 4.50 m in the vertical direction. Three spatial resolutions, described in Table 1, are considered for the simulation of the stand alone model wind turbine with fixed angular velocity of the rotor and the middle resolution is used for the case with three model wind turbines. In each spatial resolution, the domain is uniformly divided in the streamwise and spanwise direction (Nx and Ny grid cells respectively), while a stretched grid is used in the vertical direction with Nz grid cells, covering Nz_{Rotor} grid cells in one vertical rotor diameter. A zero velocity gradient is imposed at the outlet and a wall model based on the log law is

Table 1: Numerical setup.

Spatial resolution	Nx	Ny	Nz	$\Delta x(m)$	$\Delta y(m)$	$z_{min}(m)$	$R/\Delta x$	$R/\Delta y$	Nz_{Rotor}
R0	256	64	64	0.107	0.086	0.035	5.1	6.4	22
R1	384	96	80	0.072	0.057	0.022	7.7	9.6	30
R2	512	128	108	0.054	0.043	0.016	10.2	12.8	40

used to compute the stress at the surface while periodic conditions are used in the lateral boundaries. The Crank-Nicolson scheme is used to advance in time with a time step of 0.005s and the scale dependent dynamic Smagorinsky model with local averaging scheme is used to compute the subgrid scale stress, as in previous studies [17, 20] where better results were obtained with this subgrid scale model. The convective term is approximated by an implicit term and an explicit deferred correction, combining a third order compact scheme with a fourth order central difference compact scheme [31]. The inflow condition is obtained from a

precursor simulation, taking into account the same numerical setup but without wind turbine and applying a periodic boundary condition in the west and east boundaries and a constant pressure gradient as forcing term. The model wind turbine is placed $2D$ from the inlet.

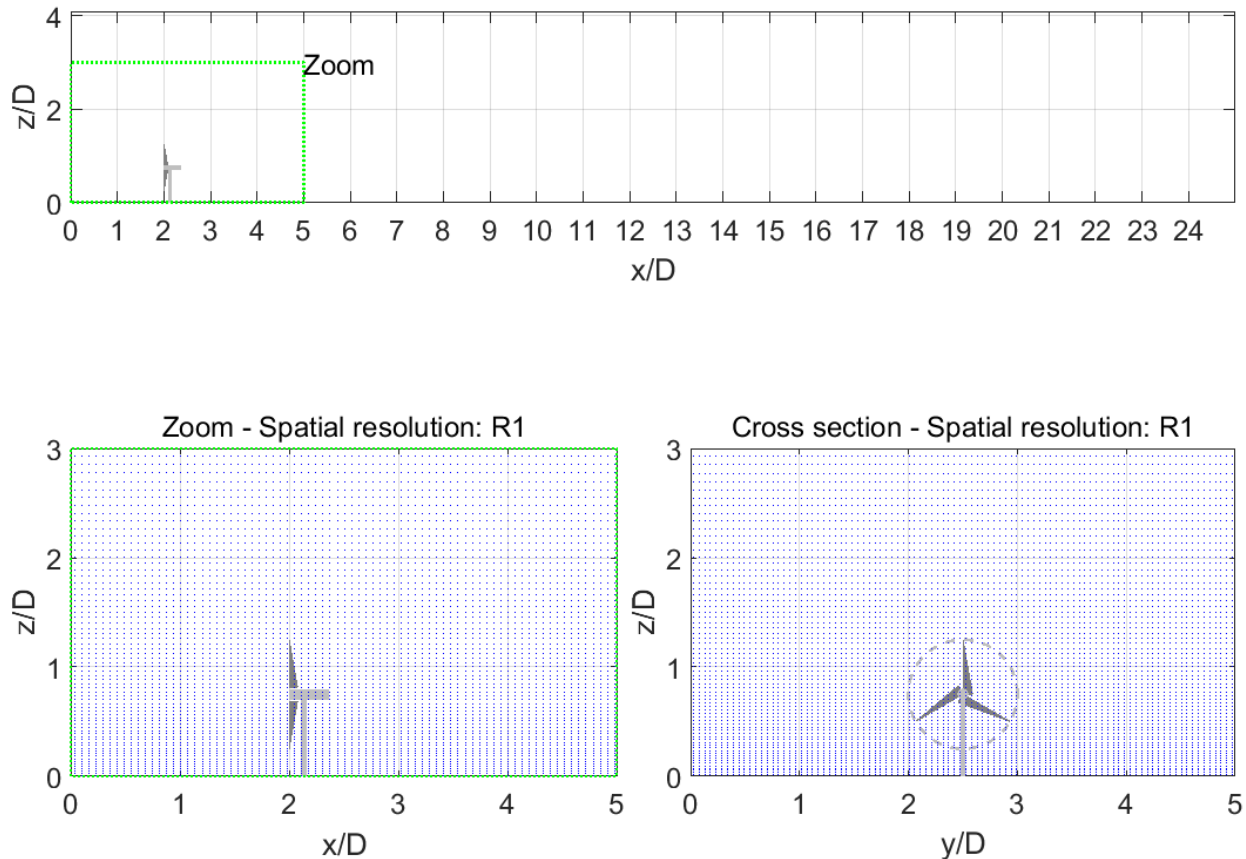


Figure 5: Side view of the computational domain (top). Spatial resolution R1: zoom view close to model wind turbine (bottom, left) and cross section (bottom, right). Blue dots represent grid node centers.

To represent the wind turbine rotor, the ALM is used with 10 radial sections in each line. The chord and twist angle are obtained from the technical data of the model wind turbine. The airfoil used is the RG14 for the entire blade. Prandtl’s tip loss correction factor is applied, as it has shown to improve the results [17]. A Gaussian smearing function is used to project the aerodynamic forces onto the computational domain, taking into account three smearing parameters (one for each direction: normal to the rotor plane, tangential and along the blade), as described in [18].

The nacelle as well as the wind turbine tower are represented through drag coefficients, see for instance [21], using a 3D smearing Gaussian function to project the forces onto the computational domain.

4.1.2 Numerical results

In this Section, numerical results obtained with the numerical framework described above are presented, comparing them with high-resolution wind tunnel measurements and focusing on wake characteristics (mean streamwise velocity component and turbulence intensity) and integral quantities to assess wind turbine performance (power and thrust coefficients).

First, the mean streamwise velocity component is analyzed. Figure 6 depicts contours of the mean streamwise velocity component in a vertical plane passing through the rotor center along the streamwise direction for the three spatial resolutions considered. That figure shows the wake deficit downstream the

rotor, characterized by a large velocity deficit in the wake center and extending beyond $10D$ downstream. The results from spatial resolutions R1 and R2 are quite close, while the results obtained with the coarser spatial resolution, exhibit a larger maximum velocity deficit. This is more clear when seeing Figure 7 where profiles of the mean streamwise velocity component at different locations in the wake from the rotor plane are presented, comparing the results of the different spatial resolutions considered and the experimental data. A good agreement is achieved with all the spatial resolutions assessed, obtaining better results with grids R1 and R2 particularly in the wake center. This could be related to the simple model used to represent the nacelle and tower, as it has shown to have a significant influence in the simulation of similar experimental setups [12]. Regarding the turbulence intensity, Figure 8 presents contours of the turbulence intensity in a

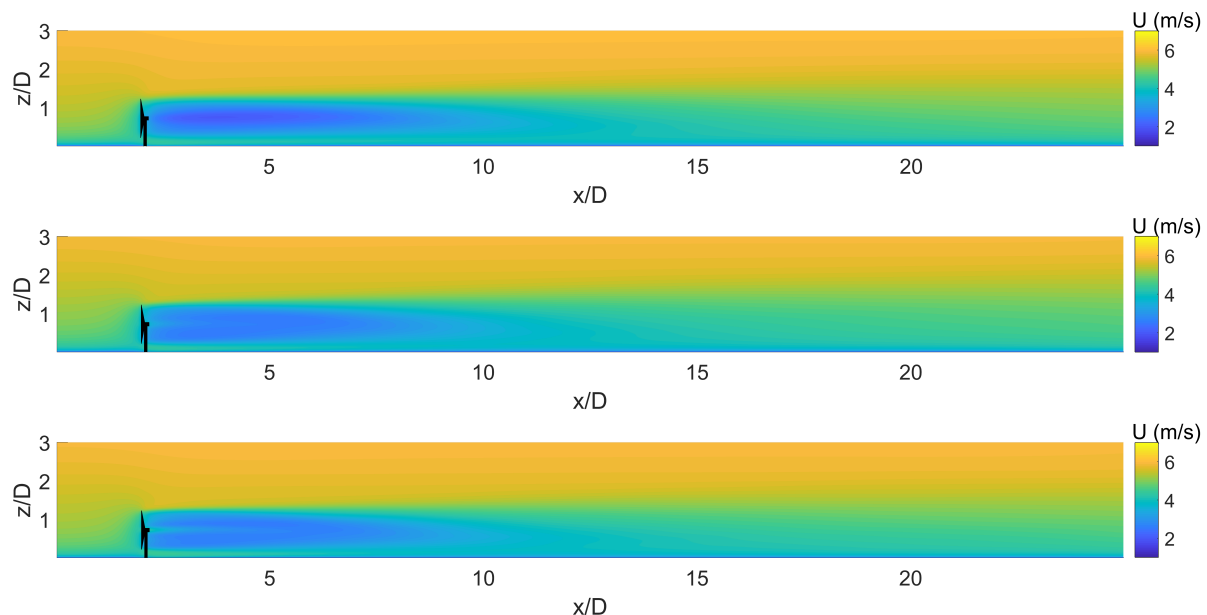


Figure 6: Mean streamwise velocity component in a plane passing through the rotor center. Top: spatial resolution R0, center: spatial resolution R1, bottom: spatial resolution R2. The model wind turbine is sketched in black.

vertical plane passing through the rotor center along the streamwise direction for the three spatial resolutions considered. In all cases, the maximum turbulence intensity is obtained at the top tip height as presented in [21, 20], while a zone of high turbulence intensity extends to almost $6D$ downstream from the rotor plane. The coarser spatial resolution predicts a larger zone of high turbulence intensity, probably related to the fact that the spatial resolution is too coarse (please see Table 1). When looking at the turbulence intensity profiles at different locations in the wake from the rotor plane in Figure 9, the difference between grid R0 and grids R1 and R2 is more clear, achieving an acceptable agreement with the latter. Close to the rotor plane, at $2D$, the differences between the experimental data and the results of the simulations, are larger, a similar observation has been presented in [20, 45, 46]. Nevertheless, the results from R1 and R2 are fair enough considering similar approaches [13, 14, 15, 16]. Finally, in this Section, integral quantities are presented in Table 2, which shows the power coefficient and thrust coefficient computed with each spatial resolution. There is a reasonable agreement in the power coefficient with the experimental data for grids R0 and R1, while spatial resolution R2 underestimates it. It should be mentioned that the inflow generated by the wind tunnel is not homogeneous in the spanwise direction, with variations in flow velocity up to 6% [43], while the experimental power coefficient is computed with the average wind speed measured by a Pitot tube located upwind from the wind turbine. On the other hand, there is a variation in the numerical power coefficient obtained with the spatial resolutions considered. It is well known that the power coefficient obtained with the ALM depends on the smearing factor used, as well as on the spatial resolution [47, 17], among other

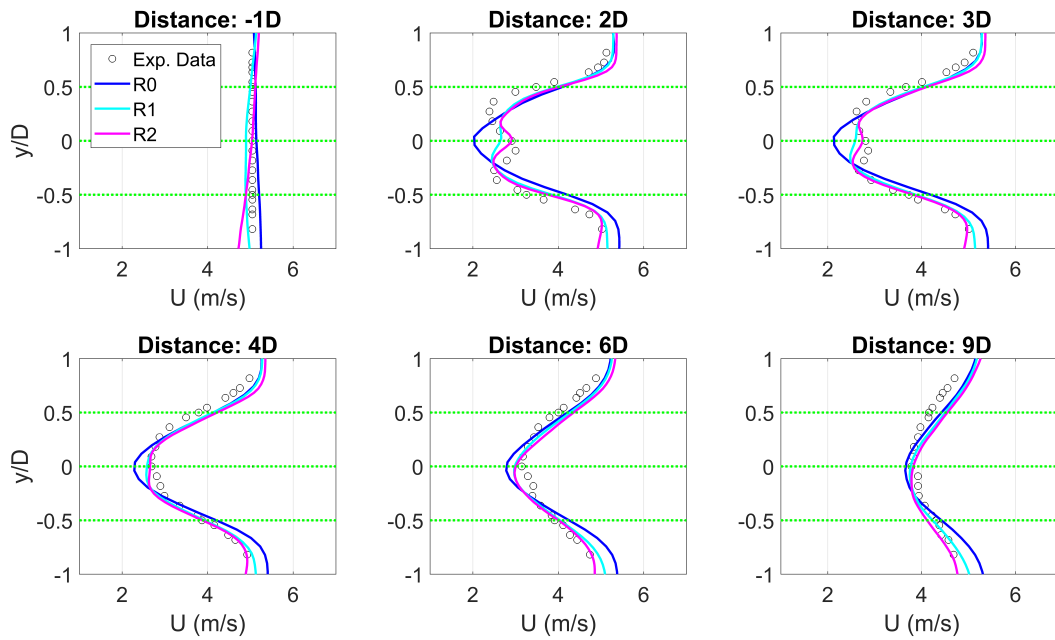


Figure 7: Mean streamwise velocity component at different locations in the wake at hub height, for the three spatial resolutions considered. Dotted green lines represent the rotor center and blade tips. Open circles represent experimental data.

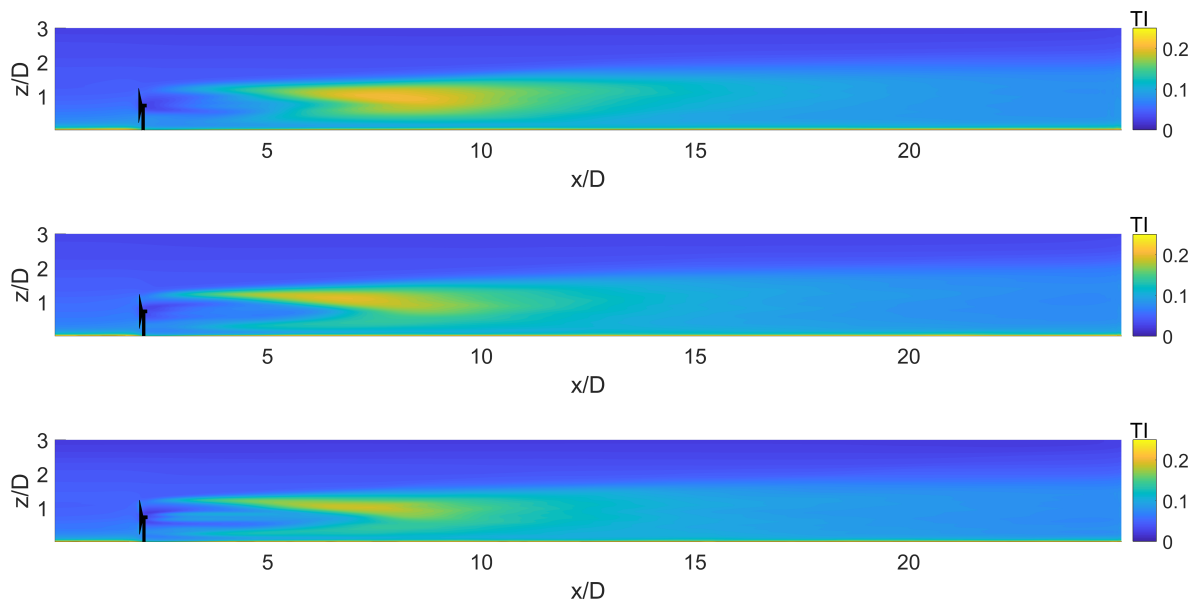


Figure 8: Turbulence intensity in a plane passing through the rotor center. Top: spatial resolution R0, center: spatial resolution R1, bottom: spatial resolution R2. The model wind turbine is sketched in black.

things. In addition to this, each power coefficient is computed taking into account the mean streamwise velocity component in the inlet boundary at hub height in front of the rotor (averaging one rotor diameter in the spanwise direction) and the inlet boundary conditions are obtained from different precursor simulations.

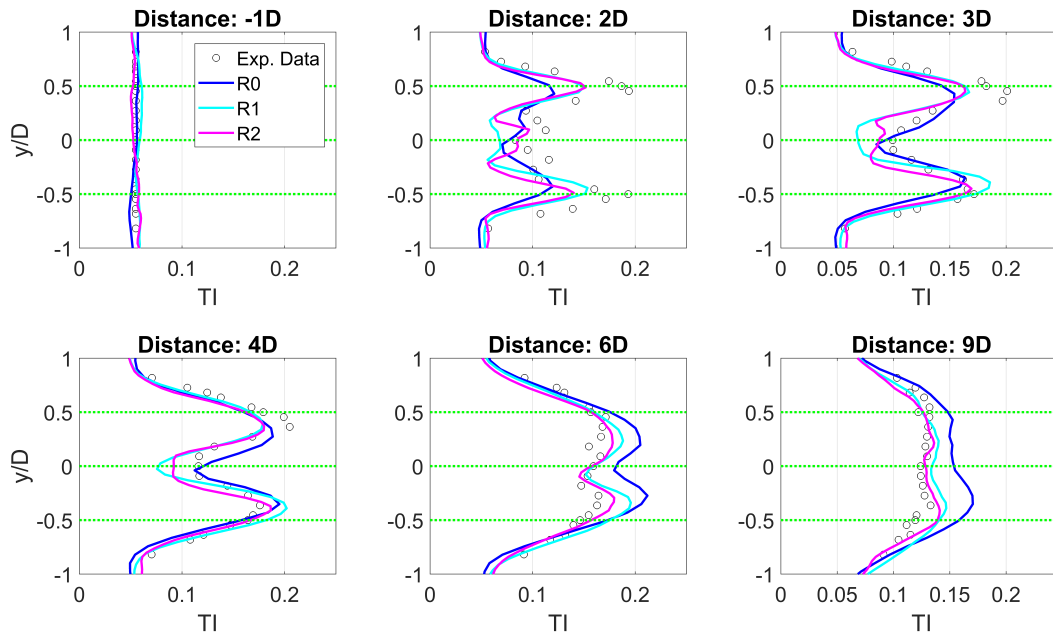


Figure 9: Turbulence intensity at different locations in the wake at hub height, for the three spatial resolutions considered. Dotted green lines represent the rotor center and blade tips. Open circles represent experimental data.

Table 2: Power and thrust coefficients. Values in brackets represent the difference between experimental and simulated value.

		C _p	C _t
Exp. Data		0.453	0.788
Sim.	R0	0.451 (-0.3%)	0.717 (-9.0%)
	R1	0.428 (-5.4%)	0.716 (-9.2%)
	R2	0.414 (-8.5%)	0.699 (-11.3%)

4.2 Three model wind turbines

In this Section another case is simulated consisting of 3 model wind turbines G1, separated $4D$ in the streamwise direction and with a lateral shift of half a diameter. During the experimental campaign each model wind turbine is operated with the torque controller and pitch control on, nevertheless the pitch value is almost fixed to 0.42° . An ABL like inlet condition is used, with a mean streamwise velocity component of 5.67 m/s and turbulence intensity of approx. 5.0% at hub height and a shear exponent of the potential law equal to 0.08 [44]. This configuration is the same as the one used in [26] to study a close-loop wind farm control development to maximize power production.

In this paper, the optimal yaw setting obtained in [26] is evaluated, in which the yaw offset of the first and second wind turbines in the streamwise direction is 20° and 16° respectively. Figure 10 depicts

the simulated configuration taking into account the yaw setup. It should be mentioned that, during the experimental campaign, the pitch control acted in the third model wind turbine, while this is not included in the numerical simulation.

The numerical setup described in Section 4.1.1, using only spatial resolution R1, is used. The inlet condition is obtained from a different precursor simulation adjusting the pressure gradient forcing term according to the experimental ABL profile. The model wind turbines are simulated operating with torque controller but without pitch control. A pitch control has been implemented recently in the code.

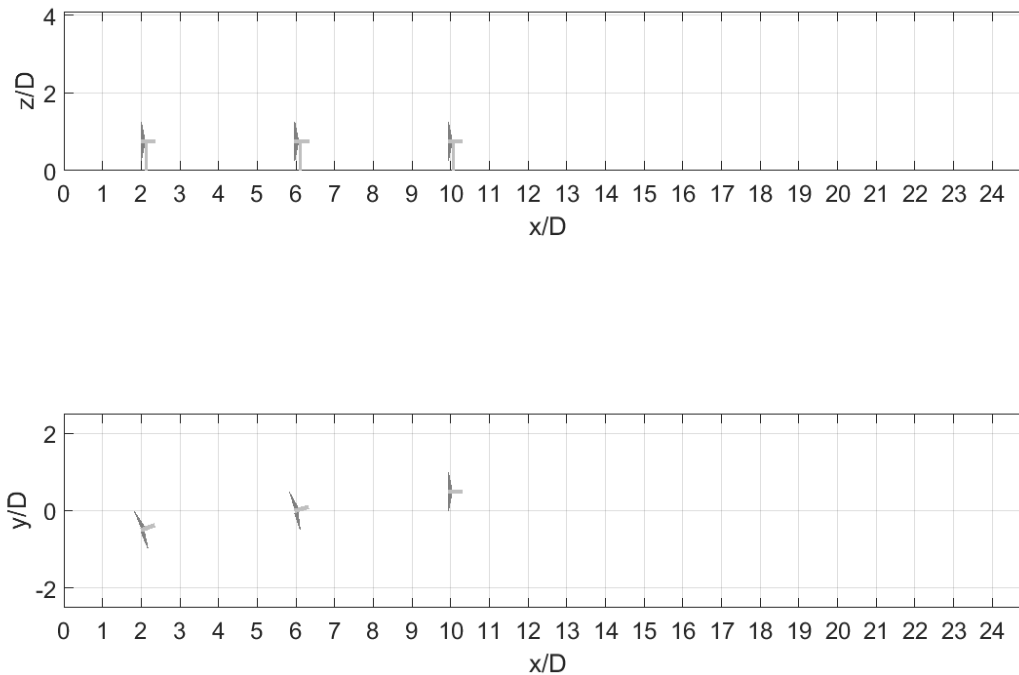


Figure 10: Computational domain showing the layout for the selected yaw setting. The wind turbine models are sketched in grey.

The mean streamwise velocity component in a horizontal plane 0.10 m above hub height is depicted in Figure 11. It can be seen that, when operating the first and second model wind turbines with yaw offset, the wake after the first one is deviated to the right when seeing from an upstream position as expected. In this case the inflow near the second model wind turbine has more kinetic energy, so an increase in its power production would be expected depending on its yaw setting. A similar result is obtained when observing the evolution of the wake of the second model wind turbine, but with a larger deviation to the right related to the fact that the spanwise velocity component upstream of it has a negative value caused by the yaw setting of the first model wind turbine (not shown here). The evolution of the wake center position along the streamwise direction obtained from the experimental data, is represented in the figure with a white dashed line. To define the wake center position, a similar approach as the one presented in [48] (based on the available mean specific power in the wind), is used, but in this case the wake center position is computed by minimization of Equation 7. From the figure it can be observed that the numerical results follow the general

trend observed in the wake center evolution found in the experimental data.

$$f_{wc}(y) = \int_{y-\frac{D}{2}}^{y+\frac{D}{2}} u^3(y') dy' \quad (7)$$

Figure 12 depicts the horizontal profile of the mean streamwise velocity component at different locations in the wake 0.10 m above hub height, including the numerical results as well as the experimental data. The spanwise position of the rotor center of each model wind turbine is represented with a green dashed line. The agreement between the numerical results and the experimental data is very good. The effect of yawing the model wind turbines is clearly seen in the velocity profiles, confirming the potential to deviate the wake generated from an upstream wind turbine on downstream wind turbines with the aim of maximizing wind power generation.

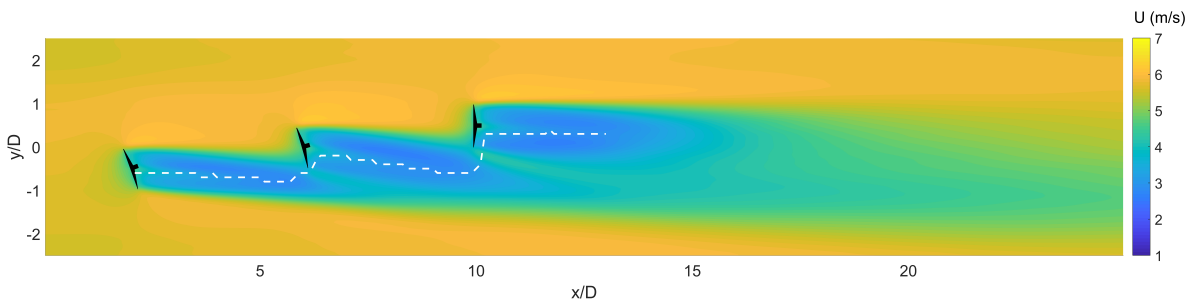


Figure 11: Mean streamwise velocity component in a horizontal plane passing 0.10 m above the rotor center. Spatial resolution R1. The model wind turbines are sketched in black. The white dash line represents the wake center computed from the experimental data by minimization of Equation 7.

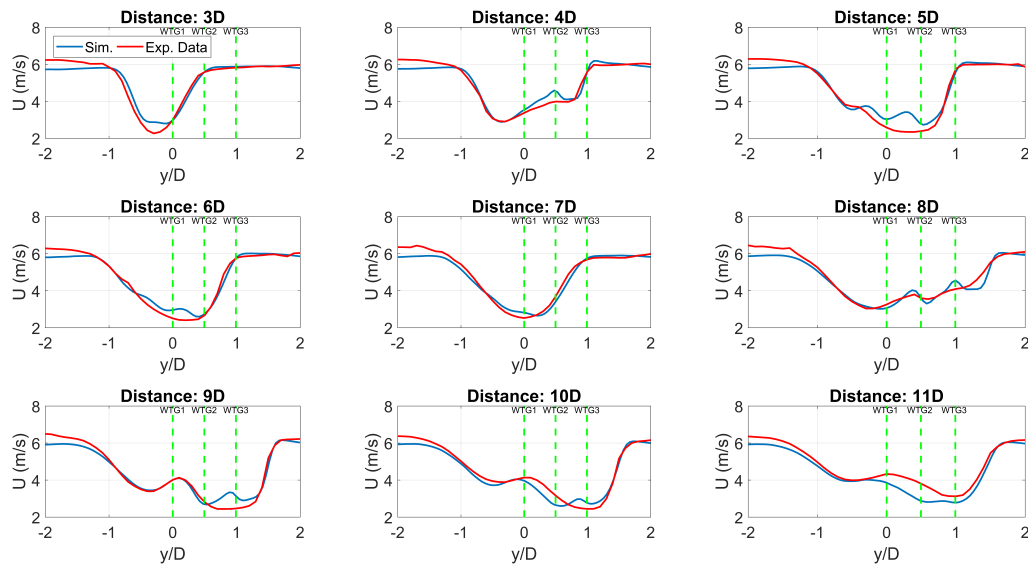


Figure 12: Mean streamwise velocity component in a horizontal plane 0.10 m above the rotor center at different locations in the wake. Spatial resolution R1. The wind turbine rotor centers are represented with green dashed lines. Distance is measured from the rotor plane of the upwind model wind turbine.

Regarding integral quantities, Figure 13 presents the power coefficient, the mean angular velocity and the mean fore-aft bending moment (M_{FA}) for each model wind turbine, including the experimental values in green. The general trend is well captured in all cases. Power coefficients are overestimated, the larger error is obtained in the third model wind turbine while the smaller error is obtained in the first model wind turbine, Table 3 presents the experimental and numerical power coefficients and their difference. The mean angular velocity is well captured for the first and second model wind turbines and it is a bit overestimated in the third model wind turbine, the latter is caused by not operating the wind turbine with pitch control to regulate the angular velocity, influencing also the power computation. As mentioned before, the wind flow in the wind tunnel is not homogeneous in the spanwise direction [43] and the experimental power coefficients are computed taking into account the mean streamwise velocity measured by a Pitot tube located upstream of the first model wind turbine, affecting the computation of the power coefficients. A similar remark can be done when analyzing fore-aft bending moment.

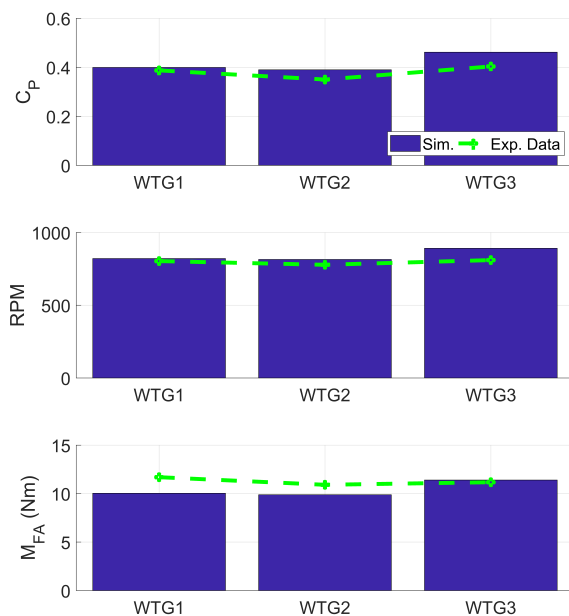


Figure 13: Power coefficient (top), rotor angular velocity (RPM , center), fore-aft bending moment (bottom). Spatial resolution R1.

Table 3: Power coefficient of each model wind turbine.

	WTG1	WTG2	WTG3	Total
Exp. Data	0.388	0.350	0.404	1.142
Sim.	0.400	0.390	0.462	1.251
Cp diff.	3.1%	11.3%	14.4%	9.6%

5 Conclusions

A Large Eddy Simulation framework with the Actuator Line Model to represent the wind turbine rotors has been used to simulate different state of the art experimental campaigns developed at Politecnico di Milano wind tunnel.

A stand-alone model wind turbine operating without torque controller at a fixed pitch has been simulated with three spatial resolutions, all of them coarser than what is generally recommended when using the

Actuator Line Model. In general a good agreement with the experimental data has been obtained, for the wake characteristics (mean streamwise velocity component and turbulence intensity) as well as for the power coefficient. The coarser spatial resolution overestimates the turbulence intensity despite computing with an acceptable agreement the mean streamwise velocity component. The thrust coefficient has been underestimated by the three grids.

A setup with three model wind turbines, separated $4D$ in the streamwise direction and half a diameter in the spanwise direction, has been simulated for a non-greedy yaw setting. The mean streamwise velocity component close to hub height has been analyzed comparing the numerical results with measurements performed in the wind tunnel with two short-range WindScanner lidars, obtaining a close agreement. Regarding the power coefficients, the power coefficient of each model wind turbine has been overestimated, nevertheless the general trend is well captured. Fore-aft bending moment has also been computed, achieving good results. The mean angular velocity of each model wind turbine also compares well with the experimental data.

In general, an acceptable agreement is obtained between the experimental data and the numerical results, showing an interesting complementary approach between physical and numerical simulation. Future research will focus on the use of this numerical framework to study wind farm control strategies, both for maximizing power production and for active power control. The use of GPGPU computing platform as considered in [49] is now being expanded to the full flow solver, using a dual CUDA / OpenCL syntax on top of the coarse MPI parallelization. This approach allows achieving speedups of up to 30x with respect to the CPU only solver and will be next extended to the wind turbine module routines.

References

- [1] International Renewable Energy Agency (IRENA). Renewable capacity statistics 2017. 2017.
- [2] International Energy Agency. Technology Roadmap. Wind Energy. 2013.
- [3] G. A. M. van Kuik, J. Peinke, R. Nijssen, D. Lekou, J. Mann, J. N. Sørensen, C. Ferreira, J. W. van Wingerden, D. Schlipf, P. Gebraad, H. Polinder, A. Abrahamsen, G. J. W. van Bussel, J. D. Sørensen, P. Tavner, C. L. Bottasso, M. Muskulus, D. Matha, H. J. Lindeboom, S. Degraer, O. Kramer, S. Lehnhoff, M. Sonnenschein, P. E. Sørensen, R. W. Künneke, P. E. Morthorst, and K. Skytte. Long-term research challenges in wind energy – a research agenda by the european academy of wind energy. *Wind Energy Science*, 1(1):1–39, feb 2016.
- [4] B. Sande, S.P. van der Pijl, and B. Koren. Review of computational fluid dynamics for wind turbine wake aerodynamics. *Wind energy*, 14(7):799–819, 2011.
- [5] J.N. Sørensen and W.Z. Shen. Numerical modeling of wind turbine wakes. *Journal of Fluids Engineering*, 124(2):393, 2002.
- [6] F. Porté-Agel, Y.-T. Wu, H. Lu, and R.J. Conzemius. Large-eddy simulation of atmospheric boundary layer flow through wind turbines and wind farms. *Journal of Wind Engineering and Industrial Aerodynamics*, 99(4):154–168, apr 2011.
- [7] M. Churchfield, S. Lee, P. Moriarty, L.A. Martínez, S. Leonardi, G. Vijayakumar, and J. Brasseur. A large-eddy simulation of wind-plant aerodynamics. *AIAA paper*, 537:2012, 2012.
- [8] P. Jha, M. Churchfield, P. Moriarty, and S. Schmitz. Accuracy of state-of-the-art actuator-line modeling for wind turbine wakes. *AIAA Paper*, (2013-0608), 2013.
- [9] N. Troldborg, F. Zahle, P.-E. Réthoré, and N. Sørensen. Comparison of wind turbine wake properties in non-sheared inflow predicted by different computational fluid dynamics rotor models. *Wind Energy*, 18(7):1239–1250, apr 2014.
- [10] U. Ciri, G. Petrolo, M. Salvetti, and S. Leonardi. Large-eddy simulations of two in-line turbines in a wind tunnel with different inflow conditions. *Energies*, 10(6):821, jun 2017.
- [11] W. Pascal, C. Schulz, T. Lutz, and E. Krämer. Comparison of the actuator line model with fully resolved simulations in complex environmental conditions. *Journal of Physics: Conference Series*, 854:012049, may 2017.
- [12] J. Wang, D. McLean, F. Campagnolo, T. Yu, and C.L. Bottasso. Large-eddy simulation of waked turbines in a scaled wind farm facility. *Journal of Physics: Conference Series*, 854:012047, may 2017.
- [13] P.-Å. Krogstad and P.E. Eriksen. “blind test” calculations of the performance and wake development for a model wind turbine. *Renewable Energy*, 50:325–333, feb 2013.

- [14] F. Pierella, P.-Å. Krogstad, and L. Sætran. Blind test 2 calculations for two in-line model wind turbines where the downstream turbine operates at various rotational speeds. *Renewable Energy*, 70:62–77, oct 2014.
- [15] P.-Å. Krogstad, L. Sætran, and M.S. Adaramola. “blind test 3” calculations of the performance and wake development behind two in-line and offset model wind turbines. *Journal of Fluids and Structures*, 52:65–80, jan 2015.
- [16] J. Bartl and L. Sætran. Blind test comparison of the performance and wake flow between two in-line wind turbines exposed to different turbulent inflow conditions. *Wind Energy Science*, 2(1):55–76, feb 2017.
- [17] M. Draper and G. Usera. Evaluation of the actuator line model with coarse resolutions. *Journal of Physics: Conference Series*, 625:012021, jun 2015.
- [18] M. Draper, A. Guggeri, and G. Usera. Modelling one row of horns rev wind farm with the actuator line model with coarse resolution. *Journal of Physics: Conference Series*, 753:082028, sep 2016.
- [19] A. Guggeri, M. Draper, and G. Usera. Simulation of a 7.7 MW onshore wind farm with the actuator line model. *Journal of Physics: Conference Series*, 854:012018, may 2017.
- [20] M. Draper, A. Guggeri, and G. Usera. Validation of the actuator line model with coarse resolution in atmospheric sheared and turbulent inflow. *Journal of Physics: Conference Series*, 753:082007, sep 2016.
- [21] Y.-T. Wu and F. Porté-Agel. Large-eddy simulation of wind-turbine wakes: Evaluation of turbine parametrisations. *Boundary-Layer Meteorology*, 138(3):345–366, dec 2010.
- [22] S. Xie and C. Archer. Self-similarity and turbulence characteristics of wind turbine wakes via large-eddy simulation. *Wind Energy*, 18(10):1815–1838, aug 2014.
- [23] Y.-T. Wu and F. Porté-Agel. Simulation of turbulent flow inside and above wind farms: Model validation and layout effects. *Boundary-Layer Meteorology*, 146(2):181–205, jul 2012.
- [24] L.A. Martínez, M. Churchfield, and S. Leonardi. Large eddy simulations of the flow past wind turbines: actuator line and disk modeling. *Wind Energy*, 18(6):1047–1060, apr 2014.
- [25] C.L. Bottasso, F. Campagnolo, and V. Petrović. Wind tunnel testing of scaled wind turbine models: Beyond aerodynamics. *Journal of Wind Engineering and Industrial Aerodynamics*, 127(Supplement C):11 – 28, 2014.
- [26] F. Campagnolo, V. Petrović, J. Schreiber, E.M. Nanos, A. Croce, and C.L. Bottasso. Wind tunnel testing of a closed-loop wake deflection controller for wind farm power maximization. *Journal of Physics: Conference Series*, 753:032006, sep 2016.
- [27] F. Campagnolo, V. Petrović, C.L. Bottasso, and A. Croce. Wind tunnel testing of wake control strategies. In *2016 American Control Conference (ACC)*, pages 513–518, July 2016.
- [28] F. Campagnolo, V. Petrović, E. Nanos, C. Tan, C.L. Bottasso, I. Paek, H. Kim, and K. Kim. Wind tunnel testing of power maximization control strategies applied to a multi-turbine floating wind power platform. In *Proceedings of the International Offshore and Polar Engineering Conference*, June 2016.
- [29] G. Usera, A. Vernet, and J.A. Ferré. A parallel block-structured finite volume method for flows in complex geometry with sliding interfaces. *Flow, Turbulence and Combustion*, 81(3):471–495, apr 2008.
- [30] M. Mendina, M. Draper, A.P. Kelm Soares, G. Narancio, and G. Usera. A general purpose parallel block structured open source incompressible flow solver. *Cluster Computing*, 17(2):231–241, nov 2013.
- [31] J.H. Ferziger and M. Peric. *Computational Methods for Fluid Dynamics*. Springer-Verlag Berlin Heidelberg, 3 edition, 2002.
- [32] C.C. Liao, Y.W. Chang, C.A. Lin, and J.M. McDonough. Simulating flows with moving rigid boundary using immersed-boundary method. *Computers & Fluids*, 39(1):152–167, 2010.
- [33] H. Hadzic et al. *Development and application of finite volume method for the computation of flows around moving bodies on unstructured, overlapping grids*. PhD thesis, Technische Universität Hamburg, 2006.
- [34] Ž. Lilek, S. Muzaferija, M. Perić, and V. Seidl. An implicit finite-volume method using nonmatching blocks of structured grid. *Numerical Heat Transfer*, 32(4):385–401, 1997.
- [35] J. Smagorinsky. General circulation experiments with the primitive equations: I. the basic experiment. *Monthly weather review*, 91(3):99–164, 1963.
- [36] P.J. Mason and D.J. Thomson. Stochastic backscatter in large-eddy simulations of boundary layers. *Journal of Fluid Mechanics*, 242:51–78, 1992.
- [37] M. Germano, U. Piomelli, P. Moin, and W.H. Cabot. A dynamic subgrid-scale eddy viscosity model.

- Physics of Fluids A: Fluid Dynamics*, 3(7):1760–1765, 1991.
- [38] Y. Zang, R.L. Street, and J.R. Koseff. A dynamic mixed subgrid-scale model and its application to turbulent recirculating flows. *Physics of Fluids A: Fluid Dynamics*, 5(12):3186–3196, 1993.
- [39] F. Porté-Agel, C. Meneveau, and M.B. Parlange. A scale-dependent dynamic model for large-eddy simulation: application to a neutral atmospheric boundary layer. *Journal of Fluid Mechanics*, 415:261–284, 2000.
- [40] E.A. Bossanyi. The design of closed loop controllers for wind turbines. *Wind Energy*, 3(3):149–163, 2000.
- [41] C. Lyon, A. Broeren, P. Gigure, A. Gopalarathnam, and M. Selig. Summary of low-speed airfoil data - vol. 3. 1998.
- [42] C.L. Bottasso, S. Cacciola, and X. Iriarte. Calibration of wind turbine lifting line models from rotor loads. *Journal of Wind Engineering and Industrial Aerodynamics*, 124(Supplement C):29 – 45, 2014.
- [43] J. Wang, S. Foley, E.M. Nanos, T. Yu, F. Campagnolo, C.L. Bottasso, A. Zanotti, and A. Croce. Numerical and experimental study of wake redirection techniques in a boundary layer wind tunnel. *Journal of Physics: Conference Series*, 854:012048, may 2017.
- [44] M.F. van Dooren, F. Campagnolo, M. Sjöholm, N. Angelou, T. Mikkelsen, and M. Kühn. Demonstration and uncertainty analysis of synchronised scanning lidar measurements of 2d velocity fields in a boundary-layer wind tunnel. *Wind Energy Science Discussions*, pages 1–17, jan 2017.
- [45] S. Xie and C. Archer. Self-similarity and turbulence characteristics of wind turbine wakes via large-eddy simulation. *Wind Energy*, 18(10):1815–1838, 2015.
- [46] R. Stevens, L.A. Martínez, and C. Meneveau. Comparison of wind farm large eddy simulations using actuator disk and actuator line models with wind tunnel experiments. *Renewable Energy*, 116:470–478, 2018.
- [47] L.A. Martínez, S. Leonardi, M. Churchfield, and P. Moriarty. A comparison of actuator disk and actuator line wind turbine models and best practices for their use. *AIAA Paper*, 900, 2012.
- [48] L. Vollmer, G. Steinfeld, D. Heinemann, and M. Kühn. Estimating the wake deflection downstream of a wind turbine in different atmospheric stabilities: an LES study. *Wind Energy Science*, 1(2):129–141, sep 2016.
- [49] P. Igounet, P. Alfaro, G. Usera, and P. Ezzatti. Towards a finite volume model on a many-core platform. *International Journal of High Performance Systems Architecture* 12, 4(2):78–88, 2012.